Mode broadening induced by nanoparticles in an optical whispering-gallery microcavity

Yuwen Hu,[1] Linbo Shao,[1] Stephen Arnold,[2] Yong-Chun Liu,[1] Cao-Yuan Ma,[1] and Yun-Feng Xiao[1,3,*]

[1]*State Key Laboratory for Mesoscopic Physics and School of Physics, Peking University, Beijing 100871, People's Republic of China*

[2]*New York University Polytechnic School of Engineering, Brooklyn, New York 11201, USA*

[3]*Collaborative Innovation Center of Quantum Matter, Beijing 100871, People's Republic of China*

(Received 28 May 2014; revised manuscript received 29 August 2014; published 21 October 2014)

We theoretically investigate mode broadening of a high-Q optical whispering-gallery microcavity coupled to a single or multiple dielectric or plasmonic subwavelength particles. The result shows that backscattering contributes dominantly to the mode broadening in both transmission and reflection spectra for dielectric particles binding on the microcavity surface, while absorption also plays an important role for lossy nanoparticles. The mode broadening induced by nanoparticles holds great potential in optical biosensing. For instance, by monitoring the change of mode linewidth, a single 11-nm-radius spherical polystyrene nanoparticle is detectable. This detection breaks through the detection limit of the mode-splitting method using a passive cavity and remains immune to various noises, such as thermal fluctuations and frequency drifts of the probe laser. Finally, the mode broadening is demonstrated to be particularly suitable for detecting lossy nanoparticles, e.g., plasmonic particles.

DOI: 10.1103/PhysRevA.90.043847 PACS number(s): 42.60.Da, 42.65.Es, 42.25.Fx

I. INTRODUCTION

Enhanced light-matter interaction in high-Q optical whispering-gallery-mode (WGM) microresonators enables various applications ranging from fundamental physical studies to functional photonic devices [1–3]. Single and multiple subwavelength particles locating in the cavity field is one of the prominent examples. They have triggered intensive studies over the past years, such as cavity quantum electrodynamics [4–12], where a single dipole strongly couples to quantized optical fields, and highly sensitive optical sensing, where characteristics of the cavity mode can be strongly affected by a single nanoparticle or a few nanoparticles [13–18]. Different from the standing wave in Fabry-Pérot cavities, the WGM cavity supports a pair of counterpropagating modes: clockwise (CW) mode and counterclockwise (CCW) mode, which have a degenerate frequency, an identical mode field distribution, and the same polarization. Single or multiple nanoparticles binding on the cavity produce many interesting phenomena. For example, backscattering of the nanoparticles couples the originally degenerate modes and generates two new nondegenerate eigenmodes [19]. When the backscattering is relatively weaker than the cavity decay rate, corresponding to the cases of small-sized nanoparticles or relatively low-Q cavities, a mode shift emerges in the transmission and reflection spectra [20,21]. When the backscattering is comparable to the intrinsic decay of the cavity mode, these two new eigenmodes split in the transmission and reflection spectra [22–25]. Recently, it was also found that nanoparticles coupled to a WGM cavity may reach exceptional points that lead to asymmetric backscattering [17,26,27], indicate a Purcell factor [28,29], and produce highly directional emission in the far field [30–32].

In terms of the optical microcavity sensing, the detection limit down to a single nanoparticle or virus has been demonstrated experimentally by monitoring either the mode shift [33–35] or the mode splitting [14,36,37], in both air and aqueous environments. In general, the mode-shift method is of a high sensitivity and a large sensing range, whereas mode splitting is immune to various noises including environmental temperature fluctuations and frequency drift of probe laser, but it relies on ultrahigh-Q WGMs. By using plasmonic enhancement [38–43] or noise suppression methods [44–46], detection of single smaller-sized targets, such as molecules, has been realized. Recently, mode broadening showed potential in single-nanoparticle detection [47,48] without ultrahigh-Q modes, and still presented a self-referenced sensing signal. In this paper, we theoretically investigate the changes of mode linewidth in transmission and reflection spectra for dielectric and lossy nanoparticles binding on a WGM cavity surface.

The rest of this paper is organized as follows. In Sec. II, a theoretical model is provided to describe nanoparticle-induced scattering and absorption. In Secs. III and IV, the mode broadening is analyzed when single or multiple lossless dielectric nanoparticles are bound on the cavity surface, and the limit of detection is given as well. In Sec. V, the mode broadening induced by lossy particles is investigated.

II. THEORETICAL MODEL

We briefly review the interaction between nanoparticles and a high-Q WGM microcavity [16,19]. As depicted in Fig. 1(a), N subwavelength spherical scatterers with radius a are randomly bound on the equator of a toroidal microcavity [49] surface, where an optical gradient force draws the nanoparticles to the position of the highest evanescent intensity [50]. The subwavelength nanoparticles (Rayleigh scatterers) are polarized by the optical evanescent field of the WGM and described by the dipole interaction following the Wigner-Weisskopf semi-QED treatment [19]. The CW- and CCW-propagating WGMs are coupled by backscattering. If the dipole-dipole interaction among nanoparticles is neglected due to their large distances, the non-Hermitian Hamiltonian for CW and CCW modes coupling to N identical scatterers and reservoir oscillators is written as

$$H = H_0 + H_1 + H_2 + H_3, \tag{1}$$

*yfxiao@pku.edu.cn; www.phy.pku.edu.cn/~yfxiao/index.html

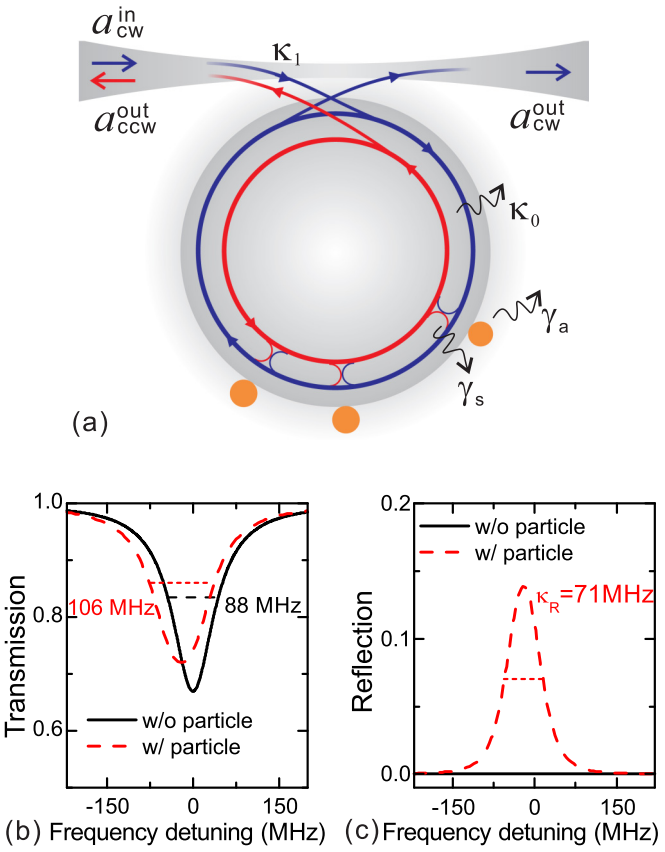

FIG. 1. (Color online) (a) Schematic diagram of a WGM cavity coupled to N subwavelength-sized particles. A tapered fiber is used to excite the cavity and collect its emission. (b) The transmission spectra of the coupling system in the undercoupling condition, i.e., $\kappa_1 = 0.1\kappa_0$, for the loaded quality factor of a cavity mode, $Q_L = 5 \times 10^6$. The black solid curve plots the transmission spectrum without particle binding, and the linewidth is 88 MHz. The red dashed curve is the transmission spectrum with one 50-nm-radius particle binding, and the linewidth increases to about 106 MHz. (c) The reflection spectra in the critical coupling condition ($\kappa_1 = \kappa_0$) for the same cavity. The black solid curve plots the reflection spectrum without particle binding, while the red dashed curve shows the spectrum with one 50-nm-radius particle binding, and the linewidth is about 71 MHz.

where

$$H_0 = \sum_{m=\mathrm{cw,ccw}} \hbar\omega_c a_m^\dagger a_m + \sum_j \hbar\omega_j b_j^\dagger b_j, \tag{2a}$$

$$H_1 = \sum_{n=1}^{N} \sum_{m,m'=\mathrm{cw,ccw}} \hbar g e^{i(k_{m'}-k_m)x_n} a_m^\dagger a_{m'}, \tag{2b}$$

$$H_2 = \sum_{n=1}^{N} \sum_{m=\mathrm{cw,ccw}} \sum_j \hbar(G_{n,m,j} a_m^\dagger b_j + \mathrm{H.c.}), \tag{2c}$$

$$H_3 = -i \sum_{n=1}^{N} \sum_{m,m'=\mathrm{cw,ccw}} \hbar \frac{\gamma_a}{2} e^{i(k_{m'}-k_m)x_n} a_m^\dagger a_{m'}. \tag{2d}$$

Here H_0 is the free Hamiltonian for the uncoupled system without intrinsic scattering, where ω_c denotes the degenerate frequency of CW and CCW WGMs without any particle binding on the cavity, and a_m (b_j) stands for the annihilation operator of the mth propagating mode (the jth reservoir mode with frequency ω_j). H_1 corresponds to the interaction between the CW and CCW modes with the strength $g = -\mathrm{Re}[\alpha] f^2(\vec{r})\omega_c/2V_m$, resulting from the particle-induced backscattering and forward scattering, where $f(\vec{r})$ is the cavity mode function; V_m is the mode volume; $\alpha = 3V_p\epsilon_1(\epsilon_p - \epsilon_1)/(\epsilon_p + 2\epsilon_1)$ is the polarizability of a particle obtained from the Wigner-Weisskopf semi-QED treatment, with V_p being the volume of the particle and ϵ_p ($\epsilon_1 = 1$) representing the relative permittivity of the nanoparticle (the surrounding medium, air in the current case). k_m is the wave vector with $k_{\mathrm{cw}} = k$ and $k_{\mathrm{ccw}} = -k$, and x_n represents the position of the nth scatterer along the CW mode traveling direction. H_2 describes the coupling between the optical cavity field and the reservoir, where $G_{n,m,j}$ is the coupling constant and H.c. stands for the Hermitian conjugation. H_3 is the cavity loss due to the particle absorption with the coefficient γ_a.

The coupling to the reservoir is equivalent to the scattering loss of the cavity modes [19], and the effective Hamiltonian H_2 reads

$$H_{2,\mathrm{eff}} = -i \sum_{n=1}^{N} \sum_{m,m'=\mathrm{cw,ccw}} \hbar \frac{\gamma_s}{2} e^{i(k_{m'}-k_m)\cdot x_n} a_m^\dagger a_{m'}, \tag{3}$$

where $\gamma_s = |\alpha|^2 f^2(\vec{r})\omega_c{}^4/6\pi v^3 V_m$ represents the scattering loss rate with v being the speed of light in the cavity.

Thus, the Heisenberg equations of motion describing the evolution of the propagating CW and CCW cavity modes become

$$\dot{a}_{\mathrm{cw}} = -i(\omega_c + Ng)a_{\mathrm{cw}} - \frac{\kappa_{01} + \gamma_a + \gamma_s}{2} a_{\mathrm{cw}} - \sum_{n=1}^{N} e^{-2ik_{\mathrm{cw}}x_n} \left(ig + \frac{\gamma_s + \gamma_a}{2} \right) a_{\mathrm{ccw}} + i\sqrt{\kappa_1} a_{\mathrm{cw}}^{\mathrm{in}}, \tag{4}$$

and

$$\dot{a}_{\mathrm{ccw}} = -i(\omega_c + Ng)a_{\mathrm{ccw}} - \frac{\kappa_{01} + \gamma_a + \gamma_s}{2} a_{\mathrm{ccw}} - \sum_{n=1}^{N} e^{-2ik_{\mathrm{ccw}}x_n} \left(ig + \frac{\gamma_s + \gamma_a}{2} \right) a_{\mathrm{cw}}, \tag{5}$$

where $\kappa_{01} \equiv \omega_c/Q_L \equiv \kappa_0 + \kappa_1$ with Q_L being the loaded quality factor of the bare cavity mode, κ_0 representing the intrinsic loss, and κ_1 standing for the coupling strength between the tapered fiber and the cavity, as shown in Fig. 1(a). Due to the backscattering of particles, the degenerate CW and CCW modes couple to each other and generate two new eigenmodes with eigenfrequencies

$$\omega_\pm = \left(\omega_c + g_\pm - i\frac{\kappa_{01} + \gamma_{\mathrm{ex}}^\pm}{2} \right). \tag{6}$$

Here $g_\pm$ describes the respective mode shift of the two eigenmodes with respect to the originally degenerate frequency ω_c, which reads

$$g_\pm = Ng \pm \mathrm{Re}[M], \tag{7}$$

where

$$M = \left(\sum_{n=1}^{N} e^{2ikx_n} \sum_{n=1}^{N} e^{-2ikx_n}\right)^{\frac{1}{2}} \left(g - i\frac{\gamma_s + \gamma_a}{2}\right), \quad (8)$$

and $\gamma_{ex}^{\pm}$ represents the extra loss of the eigenmodes induced by both scattering and absorption,

$$\gamma_{ex}^{\pm} = N(\gamma_s + \gamma_a) \mp 2\,\mathrm{Im}[M]. \quad (9)$$

Equations (7) and (9) indicate that the frequency shifts and the extra losses of the two eigenmodes are distinct, and their contributions to the mode shift, splitting, and broadening have been reported [14,20,33,47]. Conventionally, these mode characteristics are studied by measuring the transmission (defined as $T \equiv |\langle a_{cw}^{out}\rangle/\langle a_{cw}^{in}\rangle|^2$) and the reflection (defined as $R \equiv |\langle a_{ccw}^{out}\rangle/\langle a_{cw}^{in}\rangle|^2$) of the cavity. In this paper, we focus on the mode broadening $\Delta\kappa_T$. According to the input-output relation [51], the transmission and reflection are obtained as

$$T = \left|1 - \frac{\kappa_1}{2}\sum_{p=\pm}\left[i(g_p - \Delta) + \frac{\kappa_{01} + \gamma_{ex}^{p}}{2}\right]^{-1}\right|^2 \quad (10)$$

and

$$R = \left|\frac{\kappa_1}{2}\sum_{p=\pm}\mathrm{sgn}(p)\left[i(g_p - \Delta) + \frac{\kappa_{01} + \gamma_{ex}^{p}}{2}\right]^{-1}\right|^2, \quad (11)$$

where $\mathrm{sgn}(p)$ is the sign function of p, i.e., $\mathrm{sgn}(+) = 1$ and $\mathrm{sgn}(-) = -1$.

Figures 1(b) and 1(c) plot typical transmission and reflection spectra with and without a 50-nm-radius nanoparticle adsorbing on a toroidal microcavity surface, respectively. The toroidal microcavity has a major (minor) diameter of 160 μm (6 μm), the mode volume V_m is about 400 μm^3 in the air for a free space wavelength at 680 nm wavelength, and the cavity mode function $f(\vec{r})$ is about 0.26 at the particle position, similar to the parameters used in previous experiments [47]. These parameters are used throughout this paper unless specified. The transmission spectra exhibit absorption dips at the cavity resonance, and an evident mode broadening from 88 to 106 MHz is identified, in addition to a mode shift of 20 MHz. The reflection appears due to the intracavity mode scattering by the particle [45,52]. Note that both the nondegeneracy and the extra loss of eigenmodes contribute to the mode broadening $\Delta\kappa_T$ in the transmission spectrum, which is discussed in the following sections.

III. MODE BROADENING INDUCED BY A SINGLE DIELECTRIC NANOPARTICLE

First, we investigate the mode broadening induced by dielectric nanoparticles whose absorption loss is negligible, i.e., $\gamma_a = 0$. We take polystyrene (PS) nanospheres with $\epsilon_p \simeq 1.592^2$ as an example for dielectric particles throughout this paper. For dielectric nanoparticles with sufficiently small sizes, the scattering loss γ_s is typically much smaller than their coupling coefficient g, so that the mode broadening is mainly attributed to the backscattering. The spectra are reshaped by the interference of the two new eigenmodes, and thus the measured mode linewidths are subject to change in both the transmission and reflection spectra. In general, the mode broadening $\Delta\kappa$ measured in reflection spectra differs from that in transmission spectra, so we discuss them separately below.

A. Mode broadening in the transmission spectrum

In the case of a single dielectric nanoparticle binding event, substituting $\gamma_a = 0$ and $\gamma_s \ll |g|$ into Eqs. (7) and (9), we obtain $g_+ = 0$, $g_- = 2g$, $\gamma_{ex}^{+} = 0$, and $\gamma_{ex}^{-} = 2\gamma_s$. Furthermore, by substituting them into Eq. (10), the transmission spectrum is derived as

$$T = \frac{\left[-\Delta^2 + 2g\Delta + \frac{\kappa_{01}^2}{4} - \frac{\kappa_1\kappa_{01}}{2} + \frac{\kappa_0\gamma_s}{2}\right]^2 + [\kappa_0(\Delta - g) + \gamma_s\Delta]^2}{\left[-\Delta^2 + 2g\Delta + \frac{\kappa_{01}^2}{4}\right]^2 + [\kappa_{01}(\Delta - g) + \gamma_s\Delta]^2}. \quad (12)$$

Figure 2(a) plots a typical series of transmission spectra in the undercoupling regime ($\kappa_1 = 0.1\kappa_0$), when nanoparticles of different sizes are binding on the cavity. The mode splitting degrades into the mode broadening when the radius of the particle decreases. By setting $\gamma_s \sim 0$ and solving Eq. (12) at $dT/d\Delta = 0$, the minimum strength in transmission T_{min} is obtained at $\Delta \simeq g$. Thus, the full width at half maximum (FWHM) is further derived by solving $T(\Delta) = (1 + T_{min})/2$. Figure 2(b) delineates the mode broadening obtained from the transmission spectra versus the coupling coefficient g and the particle radius a. In brief, mode broadening of a small-sized particle is approximately proportional to g^2, whereas mode broadening of a larger particle, which does not induce any mode splitting yet, becomes approximately $2g$. The mode shift in the transmission spectra is also shown in Fig. 2(b) for reference. The mode shift (proportional to g) is greater than the mode broadening for a small-sized particle due to the weak backscattering described by a small coupling coefficient g. Mode broadening, however, exceeds mode shift quickly when g increases for a large-sized nanoparticle. The turning point (where mode broadening and mode shift are equal) occurs at a certain g corresponding to a critical radius of the nanoparticle and is proportional to $1/Q_L$. For example, the g at the turning points (the corresponding critical radii of particle) is ~761 MHz (169 nm), ~76.1 MHz (78 nm), ~7.61 MHz (36 nm), and ~0.761 MHz (17 nm) for modes with $Q_L = 1\times10^5$, 1×10^6, 1×10^7, and 1×10^8. However, noises are distinct in measuring mode shift and broadening, so the signal-to-noise ratios (SNRs) for mode broadening eventually determine the limit of detection, which is discussed later.

Here, to obtain a concise overview of the mode-broadening phenomena, we consider two limits.

(i) Under the low-Q or the small-sized particle limit, i.e., $\kappa_0\kappa_1 \gg g^2$, the mode broadening is reduced as

$$\Delta\kappa_T \simeq 2\left|3 - \frac{\kappa_1}{\kappa_0}\right|\frac{g^2}{\kappa_{01}}. \quad (13)$$

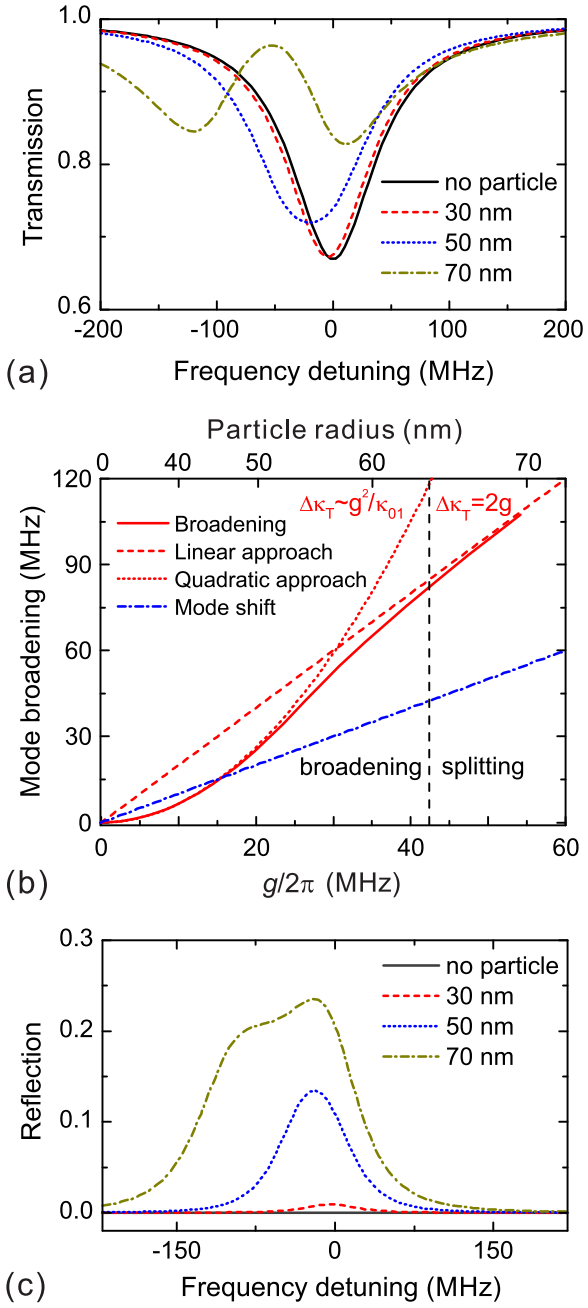

FIG. 2. (Color online) (a) Typical transmission spectra of a microcavity without and with a single 30-, 50-, or 70-nm-radius dielectric particle binding. (b) The mode broadening (red solid curve) and mode shift (blue dash-dotted curve) derived from the transmission spectra depend on the particle-induced coupling coefficient g and its radius a. The red dashed curve plots the linear approach, while the red dotted curve plots the quadratic approach of the linewidth broadening. The mode-broadening region and the mode-splitting region are separated by a black vertical line. (c) The typical reflection spectra without and with a single 30-, 50-, or 70-nm-radius dielectric particle binding. κ_R denotes the mode linewidth of the reflection spectrum. In (a)–(c), the loaded quality factor of the cavity mode is 5×10^6.

From Eq. (13), the mode broadening $\Delta\kappa_T$ is approximately proportional to both g^2 and $1/\kappa_{01}$. For instance, in the undercoupling regime of $\kappa_1 = 0.1\kappa_0$, a 30-nm-radius particle induces a 0.24-MHz mode broadening in a cavity with $Q_L = 1 \times 10^6$ (i.e., linewidth $\kappa_{01} \simeq 441$ MHz), while it produces a 2.4-MHz mode broadening for a greater $Q_L = 1 \times 10^7$ (i.e., $\kappa_{01} \simeq 44.1$ MHz). In addition, Eq. (13) indicates that mode broadening enjoys an undercoupling condition ($\kappa_1 < \kappa_0$). In the measurement of mode broadening, the SNR further enjoys a greater quality factor of a cavity mode. Assuming the uncertainty in the linewidth measurement is also proportional to the linewidth, the noise level scales down to one-tenth when Q_L increases one order of magnitude, and therefore the SNR is proportional to Q_L^2. Note here the minimum of $\Delta\kappa_T \simeq 0$ occurs at $\kappa_1/\kappa_0 = 3$, due to the mathematical definition of FWHM.

(ii) Under the high-Q or the large-sized particle limit, i.e., $\kappa_0\kappa_1 \ll g^2$, the mode further broadens and finally splits into two dips. Following the FWHM definition, the linewidth is derived by solving $T = (1 + T_{\min})/2$, although the transmission may reach the minimum elsewhere rather than at $\Delta = g$ if the mode slightly splits. In this case, the mode broadening is approximately reduced to $\Delta\kappa_T \simeq 2g$, which is consistent with the mode-splitting phenomenon. For example, we obtain a 107.5-MHz mode broadening for a 70-nm-radius particle (with $2g = 108.4$ MHz) for a cavity mode with $Q_L = 5 \times 10^6$.

Generally speaking, for small-sized particles, the mode broadening measured in a transmission spectrum is quadratic to the particle-induced coupling coefficient g and depends on both Q_L and κ_1/κ_0, whereas, for large-sized particles, the mode broadening becomes $2g$. For cases between these two conditions, i.e., $\kappa_0\kappa_1 \sim g^2$, the mode broadening shows a transition from a quadratic to a linear function of g, as shown in Fig. 2(b).

B. Mode broadening in the reflection spectrum

The mode broadening in reflection spectra $\Delta\kappa_R$ is distinct from that in transmission spectra. When there is no particle on the cavity surface and defects-induced backscattering is neglected, only the CW mode can be observed in the cavity. As shown in Fig. 1(a), the input light only couples the CW mode. In this case, due to the absence of backscattering, the CW and CCW modes do not couple. Therefore, the CCW mode is not excited, and thus the reflection rate of the cavity is zero. The mode, however, will be observed in reflection spectra when particle binding exists on the cavity. In experiments, measuring reflection spectra shows several advantages, e.g., a better SNR in the measurement [45,52]. By taking the condition of a single lossless dielectric particle into Eq. (11), the reflection spectrum is derived as

$$R = \frac{\kappa_1^2\left[\left(\frac{\gamma_s}{2}\right)^2 + g^2\right]}{\left[\Delta^2 + \left(\frac{\kappa_{01}}{2}\right)^2\right]\left[(\Delta - 2g)^2 + \left(\frac{\kappa_{01}+2\gamma_s}{2}\right)^2\right]}. \quad (14)$$

Figure 2(c) plots the typical reflection spectra of a cavity mode in the critical coupling condition ($\kappa_0 = \kappa_1$). Both the mode broadening and light strength increase are observed as expected when the particle size becomes larger. The maximum reflection rate of the reflection spectrum reaches $R_{\max} = \kappa_1^2 g^2/(g^2 + \kappa_{01}^2/4)^2$, and it reduces to $16\kappa_1^2 g^2/\kappa_{01}^4$ for a small-sized particle, indicating the maximum reflected strength proportional to g^2, and thus to r^6. In the theoretical

model, without particle binding, the initial reflection remains zero, and the linewidth is undefined, so in the following we analyze the linewidth itself instead of the linewidth variance in the reflection spectrum. Similar to the transmission case, by solving $R = (1/2)R_{\max}$, the FWHM linewidth of a reflection spectrum is derived as

$$\kappa_R = \sqrt{(2^{1/2}-1)\kappa_{01}^2 + (2g)^2}. \quad (15)$$

To make a comparison with mode broadening in transmission, we also consider the two limits.

(i) For a low-Q mode or a small-sized particle, i.e., $\kappa_{01} \gg g$, for example, and the radius a of the nanoparticle less than 65 (30) nm for $Q_L = 1 \times 10^6$ (1×10^7), the linewidth is reduced as

$$\kappa_R = \sqrt{2^{1/2}-1}\kappa_{01} + \frac{2}{\sqrt{2^{1/2}-1}}\frac{g^2}{\kappa_{01}}$$
$$\simeq 0.64\kappa_{01} + 3.1\frac{g^2}{\kappa_{01}}. \quad (16)$$

In Eq. (16), the first term is recognized as the contribution of the initial mode linewidth (κ_{01}), while the second term describes the particle-induced mode broadening, and it is proportional to both g^2 and $1/\kappa_{01}$. This result is similar to that in the transmission spectrum [Eq. (13)], but the coefficients are different.

(ii) For a high-Q mode or a large-sized particle, i.e., $g \gg \kappa_{01}$, the linewidth $\kappa_R \simeq 2g$, and the mode in the reflection spectrum begins to split when the particle radius increases, as shown in Fig. 2(c).

The transmission and reflection spectra share similar behaviors. To avoid redundancy, we mainly discuss mode broadening in the transmission spectrum. However, we should note that due to the intrinsic cavity loss of the mode, $T + R \neq 1$, mode broadenings in transmission and reflection spectra are not identical.

C. Detection limit of a single dielectric nanoparticle

Here, we discuss the detection limit of a single dielectric nanoparticle by monitoring the mode broadening $\Delta\kappa_T$ variation. One method to reduce the detection limit is to maximize the mode broadening $\Delta\kappa_T$ induced by a small-sized particle. From Eq. (13), $\Delta\kappa_T$ is determined by (1) the intrinsic loss of the cavity mode κ_0, (2) the external coupling strength between probe laser and cavity mode κ_1, as well as the ratio between them, and (3) the scattering strength g between CW and CCW modes. As stated above, a smaller κ_1/κ_0 and a higher Q_L are helpful in enhancing the mode broadening. For instance, $\Delta\kappa_T$ increases about 50% from the critical to the undercoupling condition, although too-weak coupling results in a shallow dip in the spectrum and thus reduces the SNR. In terms of the scattering strength g itself, a reduced cavity mode volume can also improve $\Delta\kappa_T$.

To reduce the detection limit, suppressing the noise in measurement serves as an alternative method. In measuring the transmission spectrum, the dominant noise sources are from electrical devices (for example, function generator, photodetector, and oscilloscope) and pump laser fluctuations, which are either white noise, Gaussian noise, $1/f$ noise, or other more complex noises. While Ref. [53] shows a treatment of noises in WGM sensing, for simplicity we consider the uncertainty of linewidth measurement proportional to the mode linewidth itself.

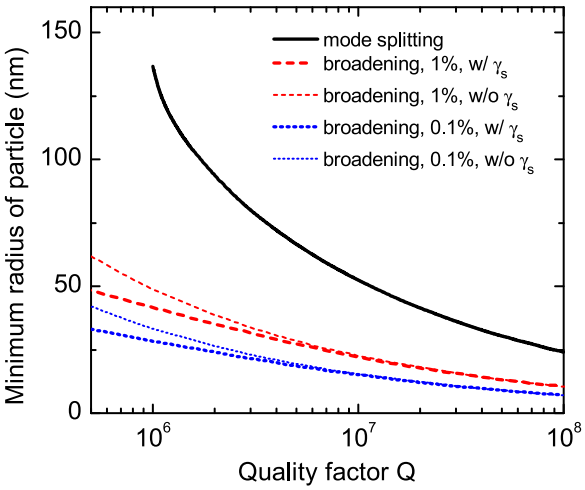

FIG. 3. (Color online) Minimum radii of single detectable particles depending on Q_L. Red dashed and blue dotted curves plot the detection limit by mode broadening with linewidth measurement uncertainty of 1% and 0.1%. Thick (thin) curves correspond to the cases with (without) considering the scattering loss γ_s. The black thick solid curve plots the detection limit by the mode-splitting method. The microcavity initially works in the undercoupling regime ($\kappa_1 = 0.1\kappa_0$).

The detection limit is determined by setting the SNR equal to one, i.e., $\Delta\kappa_T = \eta_{\text{noise}}\kappa$, where η_{noise} represents the noise level in linewidth measurements. Figure 3 plots the detection limit with noise level η_{noise} equal to 1% and 0.1% of the linewidth in the cases with or without the scattering loss γ_s, respectively. A detection noise level of 1.3% was experimentally reported in Ref. [47]. In deriving the minimum detectable radius of a single particle, when using a relatively low-Q cavity, the contribution by scattering loss γ_s becomes considerable. This is because, in such cases, the scattering loss rate is large in comparison with coupling strength g. For reference, the limit of detection for the mode-splitting method is also provided by using the condition of $2g > \kappa_{01} + \gamma_s$ [14]. Even if the nanoparticle size is large enough, the mode-splitting phenomenon will not occur for low-Q factors ($< 1 \times 10^6$), while the mode broadening can always be observed. According to Eq. (13), the minimum detectable radius of the particle is proportional to $Q_L^{-1/3}$ for a high-Q cavity. For instance, when $\eta_{\text{noise}} = 1\%$, the minimum detectable radius a of a PS particle is about 41 nm at $Q_L = 1 \times 10^6$, 22 nm at $Q_L = 1 \times 10^7$, and 11 nm at $Q_L = 1 \times 10^8$.

IV. MODE BROADENING INDUCED BY MULTIPLE DIELECTRIC PARTICLES

In this section, we study the situation of multiple nanoparticles binding on the cavity surface. Note that the relative positions of the particles play important roles in mode broadening.

A. Mode broadening induced by two particles

To simplify the discussion, we first consider two identical particles binding on the cavity with an identical coupling strength g. In this case, the transmission spectrum is obtained by setting $N = 2$ in Eq. (10), and then the mode linewidth in the transmission spectrum is derived with an additional factor $\cos^2[k(x_1 - x_2)/2]$ describing the relative position. In the small-sized particle limit, mode broadening induced by the two particles reads

$$\Delta\kappa_T \simeq 8\left|3 - \frac{\kappa_1}{\kappa_0}\right|\frac{g^2}{\kappa_{01}}\cos^2\left[\frac{k(x_1 - x_2)}{2}\right], \qquad (17)$$

where $(x_1 - x_2)$ describes the relative position of particles on the cavity. We denote the relative phase difference between two particles as $\phi = k(x_1 - x_2)$. It is evident that $\Delta\kappa_T$ exhibits cosinoidal oscillations depending on the phase factor $k(x_1 - x_2)/2$ [17,25,26,54], with an interdistance period of π/k. On the one hand, when $k(x_1 - x_2)/2 = q\pi$ (q is a nonzero integer), the mode broadening $\Delta\kappa_T$ reaches its maximum $8|3 - \kappa_1/\kappa_0|\, g^2/\kappa_{01}$, which is four times the single-particle-induced mode broadening given in Eq. (13), where both particles are exactly located at the antinodes of one eigenmode and the nodes of the other eigenmode. This maximal broadening can also be explained by the constructive interference of the fields scattered by two particles, where the wave propagates in a round trip between the two particles with a 2π phase shift. On the other hand, neglecting the ultrasmall scattering loss, mode broadening disappears when $k(x_1 - x_2)/2 = (q + 1/2)\pi$. In such cases, the second particle cancels the effect of the first particle by the destructive interference effect.

Similarly, in the small-sized particle limit, we also obtain the mode linewidth from the reflection spectrum, expressed as

$$\kappa_R \simeq \sqrt{2^{1/2} - 1}\kappa_{01} + \frac{8}{\sqrt{2^{1/2} - 1}}\frac{g^2}{\kappa_{01}}\cos^2\left[\frac{k(x_1 - x_2)}{2}\right]$$
$$\simeq 0.64\,\kappa_{01} + 12.43\,\frac{g^2}{\kappa_{01}}\cos^2\left[\frac{k(x_1 - x_2)}{2}\right]. \qquad (18)$$

Equation (18) shows that the mode linewidth is also proportional to $\cos^2[k(x_1 - x_2)/2]$. By comparing Eqs. (18) and (16), two particles, again, can reach at most four times the mode broadening induced by a single particle. These two-particle results for the transmission and reflection spectra measurement can be extended to the N particles cases, where the maximum broadening is N^2 times the single-particle-induced broadening, when they are all exactly located at the antinodes of the eigenmode. Similar results, but for the mode splitting, are also observed in Refs. [26,55].

The discussion above is for small particles; we further calculate the mode broadening for larger particles until mode splitting takes place. Figure 4(a) shows normalized mode broadening by two identical particles with different size in radius and different positions. The mode broadening is normalized by the maximum mode broadening at a certain particle radius. Figure 4(b) is the normalized mode broadening at two certain particle radii. The mode broadening induced by two 10-nm-radius particles experiences a cosinelike modulation with the period 2π. For two 50-nm-radius particles, which do not induce mode splitting, the mode broadening exhibits slightly different behavior. This cosinelike behavior of mode broadening depending on the relative particle positions covers a large range of particle radii.

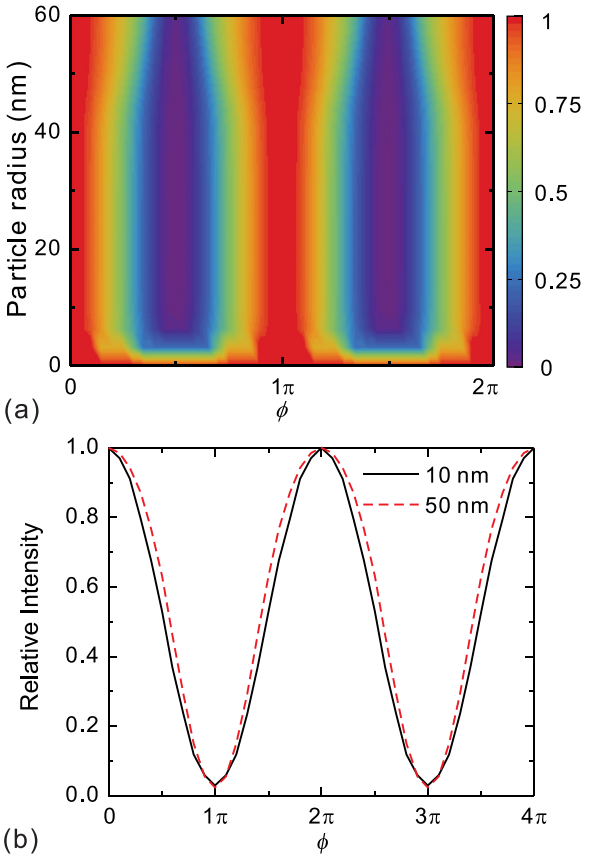

FIG. 4. (Color online) (a) Normalized mode broadening for two identical particles with different radii and relative positions. The normalized mode broadening is defined as the ratio between the mode broadening and the maximum broadening at the certain radius. (b) Normalized mode broadening for particle radii of 10 nm (black solid line) and 50 nm (red dashed line). The loaded quality factor of the cavity is $Q_L = 5 \times 10^6$.

B. Mode broadening induced by N particles

We now numerically consider the three-particle case by plotting the mode broadening as a function of relative positions of three particles. The mode broadening is normalized by the maximum mode broadening induced by a certain size of particles. The phase difference between the first and second particles is denoted as ϕ_1, and between the second and third particles as ϕ_2. The normalized mode broadening is shown in Fig. 5. A periodic variation of the linewidth depending on the relative positions among the three particles is observed.

We then investigate the case of arbitrary N nanoparticles. As expected, the mode broadening strongly depends on the position of each particle. A statistical distribution of mode broadening is obtained by randomly positioning these particles on the equator surface of the microcavity. By neglecting the scattering and absorption losses resulting from particles, the mode broadening is attributed to the difference between

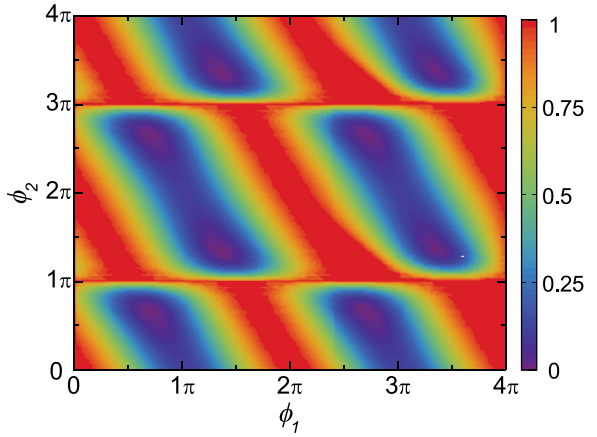

FIG. 5. (Color online) Normalized mode broadening for three identical 10-nm-radius particles with different relative positions. ϕ_1 and ϕ_2 denote the relative phase difference between the first and second particles, and between the second and third particles, respectively. The quality factor of the cavity is $Q_L = 5 \times 10^6$.

the shifts of new eigenmodes described by Eq. (7). For small-sized particles, a Monte Carlo method is employed to simulate the randomly placed positions of particles, and the expected values of mode broadening in transmission and reflection spectra read as

$$\Delta\kappa_{T,N} \simeq 1.5 \left|3 - \frac{\kappa_1}{\kappa_0}\right| \frac{Ng^2}{\kappa_{01}} \tag{19}$$

and

$$\Delta\kappa_{R,N} = \frac{2}{\sqrt{2^{1/2}-1}} \frac{g_N^2}{\kappa_{01}} \simeq 2.33 \frac{Ng^2}{\kappa_{01}}. \tag{20}$$

Figure 6(a) plots the distribution of mode broadening $\Delta\kappa_{T,N}$ induced by N identical small-sized particles. As expected, the uncertainty of $\Delta\kappa_{T,N}$ decreases when the large amount of particles increases, and the average value of broadening $\Delta\kappa_{T,N}$ arrives at about $0.75N$ times the single-particle-induced broadening. Figure 6(b) shows the mode broadening induced by N identical particles with different sizes. It is noticed that the mode broadening strongly depends on the size of the nanoparticles. As described in Eq. (19), $\Delta\kappa_{T,N}$ is proportional to g^2, and thus to r^6. Thus, tens of 20-nm-radius particles will cause a mode broadening exceeding 0.8 MHz, a typical noise level in measurement of the mode with $Q_L = 5 \times 10^6$, whereas a thousand 10-nm-radius particles are required to raise the mode broadening over the same noise level.

By comparing the mode broadening and the noise level, the limit of detection is obtained when the SNR is set to 1. The typical mode broadening is described by the statistical average of distribution in Eq. (19). When the noise level is set to 1% of the original linewidth, Fig. 7 shows the minimum detectable number of particles under various particle radii and different quality factors. For a higher quality factor, fewer particles are required to make particles detectable. For example, at least hundreds of 20-nm-radius particles are required to be detectable by a cavity mode with $Q_L = 1 \times 10^6$, but fewer particles are detectable by a cavity mode with $Q_L = 1 \times 10^7$.

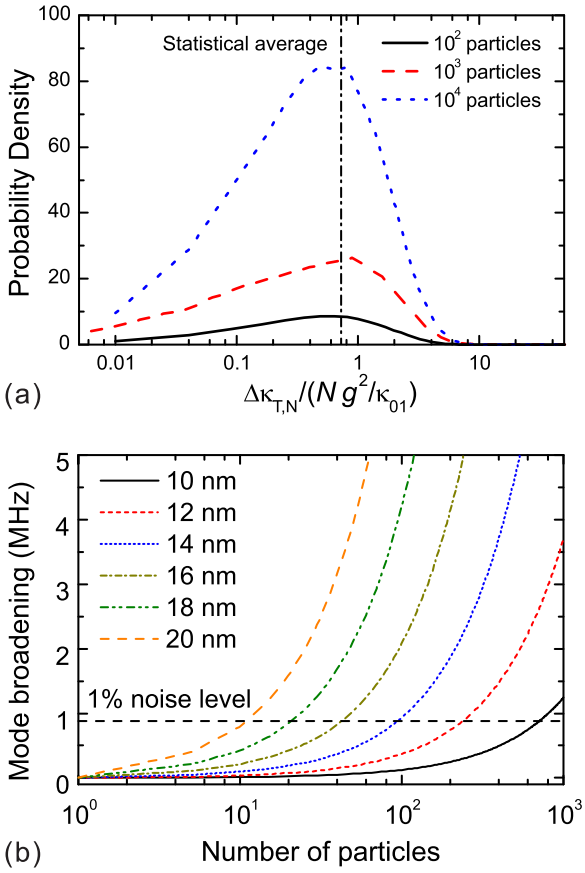

FIG. 6. (Color online) (a) Distribution of mode broadening induced by N identical dielectric particles, obtained from transmission spectra. Black solid, red dashed, and blue dotted curves correspond to $N = 1 \times 10^2$, 1×10^3, and 1×10^4. The mode broadening is normalized by Ng^2/κ_{01}. The statistical average is indicated by a vertical line at $\Delta\kappa_{T,N}/(Ng^2/\kappa_{01}) \simeq 0.75$. (b) The mode broadening induced by N dielectric particles at different particle radii from 10 to 20 nm. For both (a) and (b), $\kappa_1 = 0.1\kappa_0$, $Q_L = 5 \times 10^6$.

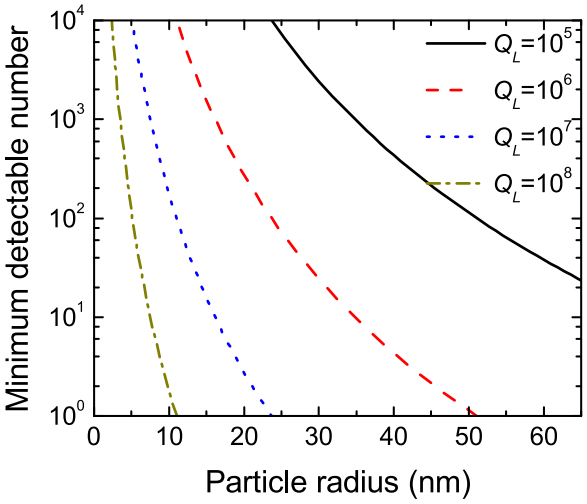

FIG. 7. (Color online) Minimum detectable number for dielectric particles with different radii. Black solid, red dashed, blue dotted, and yellow dash-dotted curves correspond to $Q_L = 1 \times 10^5, 1 \times 10^6$, 1×10^7, and 1×10^8. Here, $\kappa_1 = 0.1\kappa_0$.

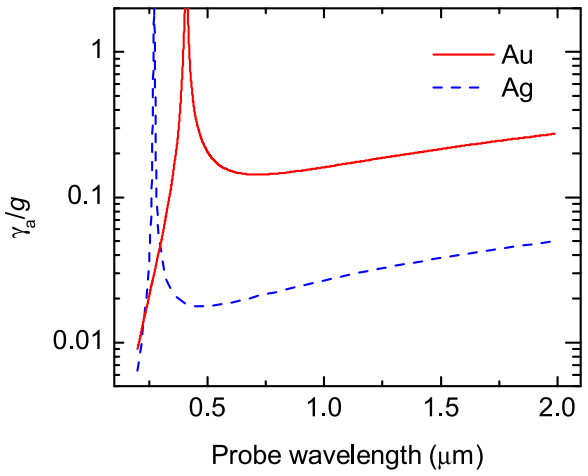

FIG. 8. (Color online) Ratio of absorption loss rate γ_a to backscattering strength g vs the probe laser wavelength for gold (red solid) and silver (blue dashed) nanospheres. Here, $\kappa_1 = 0.1\kappa_0$.

V. MODE BROADENING INDUCED BY LOSSY NANOPARTICLES

Lossy particles, such as metal targets and fluorescent markers, hold their interests in sensing experiments [35]. While the absorption loss does not improve the SNR in sensing using mode shift and mode splitting, it does broaden the mode linewidth in addition to scattering. To have a concrete view of the lossy particle-induced effects, we take metallic particles as an example. In particular, when the probe laser frequency falls into the surface plasmon resonance (SPR) (i.e., $\mathrm{Re}[\epsilon_p(\omega)] = -2\epsilon_1$ for spherical particles) of metal particles, the detection limit will be further improved by the enhanced interaction between the metal particle and the cavity mode.

A. Absorption loss of a nanoparticle

Actually, Eq. (6) has already taken the absorption of a nanoparticle into account. The permittivity of metal particles, $\epsilon_p(\omega)$, can be described by a modification of the Drude model [56], in which the imaginary part cannot be ignored. In the optical evanescent field of the cavity mode, the absorption loss of particles is obtained by [43]

$$\gamma_a = \mathrm{Im}\left[\frac{d(\omega\epsilon_p(\omega))}{d\omega}\right]\frac{f^2(\vec{r})\,\omega_c V_p}{2V_m}. \tag{21}$$

Since both the backscattering coupling strength g and the absorption loss γ_a are proportional to the volume of the particle, V_p, the ratio of γ_a to g is independent of V_p and is derived as

$$\left|\frac{\gamma_a}{g}\right| = \left|\frac{\mathrm{Im}[d\omega\epsilon_p(\omega)/d\omega]}{\mathrm{Re}[3(\epsilon_p(\omega)-\epsilon_1)/(\epsilon_p(\omega)+2\epsilon_1)]}\right|. \tag{22}$$

Figure 8 shows the dependence of $|\gamma_a/g|$ on the probe frequency ω for silver and gold nanoparticles. In a broadband wavelength, γ_a and g are comparable. At certain wavelengths centered around 410 nm for gold and 270 nm for silver, where $\mathrm{Re}[\epsilon_p(\omega)] \sim \epsilon_1$ corresponding to the case of $g \sim 0$, the absorption effect even dominates the total mode broadening. Figure 9(a) plots the mode broadenings with and without absorption loss at $\lambda = 680$ nm, and the proportion of absorption in the total mode broadening is shown in Fig. 9(b). It can be observed that the mode broadening is largely enhanced by the absorption loss. For large particles, the contribution of absorption reduces because the scattering loss cannot be ignored.

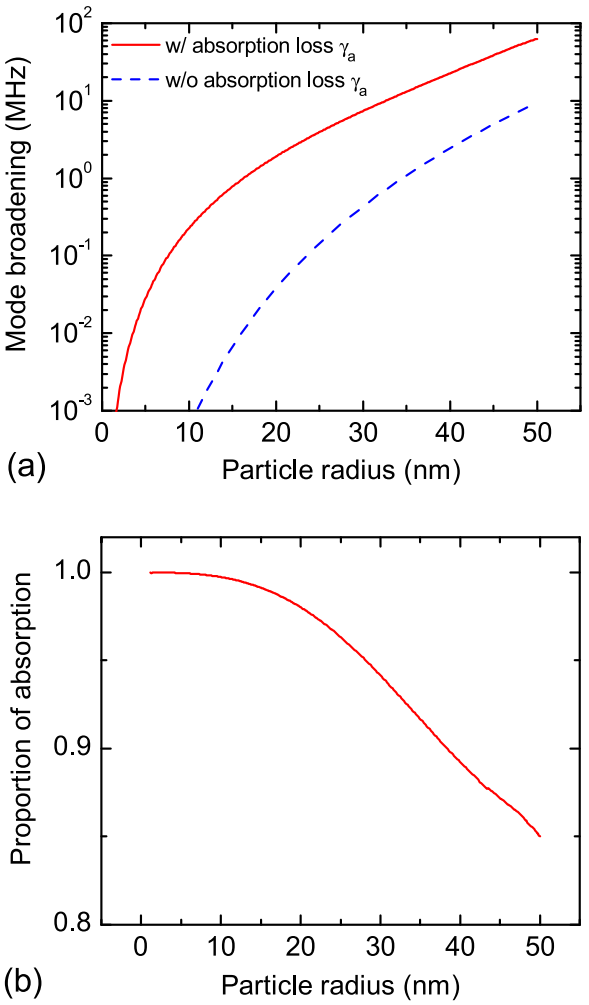

FIG. 9. (Color online) (a) Mode broadening in the transmission spectrum of a cavity with $Q_L = 5 \times 10^6$ in 680-nm wavelength. The red solid curve is mode broadening of a silver nanosphere with absorption loss, while the blue dashed curve is plotted by ignoring the contribution of absorption loss. (b) The proportion of absorption in the total mode broadening. Here, $\kappa_1 = 0.1\kappa_0$.

Since the absorption loss contributes to mode broadening as well as backscattering, the plasmonic particle requires a lower quality factor and enjoys a better limit of detection. Taking silver particles as an example, the detection limit (1% of the linewidth) for a 680-nm laser for different quality factor cavities is plotted by the red solid curve in Fig. 10. The detection limit of a single silver particle is 26.6 nm for $Q_L = 1 \times 10^6$, while it is 12.4 nm for $Q_L = 1 \times 10^7$, and 5.8 nm for $Q_L = 1 \times 10^8$.

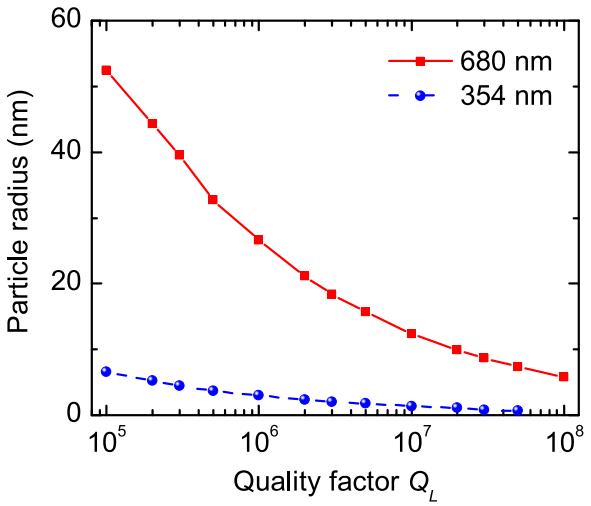

FIG. 10. (Color online) Minimum detectable radius of a single silver nanosphere at SPR (354 nm) and non-SPR (680 nm) wavelengths depending on different cavity quality factors. Here, $\kappa_1 = 0.1\kappa_0$.

B. SPR enhanced mode broadening

When the frequency of the probe laser satisfies the SPR condition, the electric field inside metallic particles will be largely amplified, and thus the enhanced particle-field interaction further broadens modes in the transmission and reflection spectra. Denoting the evanescent electric field of the cavity as E_0, the electric field inside the spherical metal particle is derived as $[3\epsilon_1/(\epsilon_p + 2\epsilon_1)]E_0$, and the polarizability of the particle is $[3(\epsilon_p - \epsilon_1)/(\epsilon_p + 2\epsilon_1)]\epsilon_0\epsilon_1 E_0$. When $\mathrm{Re}[\epsilon_p] = -2\epsilon_1$, i.e., the SPR condition, the localized electric field reaches the maximum at $3/(i\,\mathrm{Im}[\epsilon_p])E_0$. It should be noticed that only a small imaginary part of permittivity will enjoy an enhanced electric field. The modulated coupling strength is

$$g' = -\frac{1}{2}(\alpha^*\beta + \text{c.c.})\frac{f^2(\vec{r})\omega_c}{2V_m}, \tag{23}$$

where $\beta \equiv 3\epsilon_1/(\epsilon_p + 2\epsilon_1)$, and c.c. means complex conjugation. The modulated scattering loss arrives,

$$\gamma_s' = |\alpha|^2|\beta|^2\frac{f^2(\vec{r})\omega_c^4}{6\pi V_m v^3}, \tag{24}$$

and the modulated absorption loss reads

$$\gamma_a' = \mathrm{Im}\left[\frac{d(\omega\epsilon(\omega))}{d\omega}\right]|\beta|^2 V_p\frac{f^2(\vec{r})\omega_c}{2V_m}. \tag{25}$$

For silver particles, the SPR condition is satisfied at $\lambda = 354$ nm, and the imaginary part of the permittivity is about 0.6. The coupling strength g, absorption loss γ_a, and scattering loss γ_s are enhanced by about 25, 25, and 625 times those in the non-SPR case. Figure 10 plots the detection limit of a single silver nanosphere at 1% noise level depending on the quality factor Q_L. At SPR, the detection limit for $Q_L = 1 \times 10^6$ is about 3 nm and it is further reduced to 1.5 nm for $Q_L = 1 \times 10^7$, where the finite-size effect is ignored.

VI. CONCLUSION

In summary, we have theoretically studied the mode-broadening phenomenon in transmission and reflection spectra when a single nanoparticle or multiple nanoparticles are binding on a WGM microcavity. Mode broadening attributes dominantly to backscattering instead of scattering to a reservoir of dielectric nanoparticles, while the absorption of lossy nanoparticles, such as metal targets, may also play an important role. The change of cavity mode linewidth holds great potential for practical optical sensing. For instance, by monitoring the linewidth change of a cavity mode with $Q = 1 \times 10^8$, a single dielectric nanoparticle with size down to 11 nm in radius can be detected without any sensitivity enhancement mechanism or active noise control technique, showing a significantly improved limit of detection compared to the mode-splitting method in a passive microcavity. Furthermore, the absorption of target particles can increase the mode broadening, which leads to a better detection limit in particle size.

ACKNOWLEDGMENTS

We thank Yu-Feng Shen, Wei-Liang Jin, Bei-Bei Li, Yi-Wen Hu, and Xiao-Chong Yu for valuable discussions. This work was supported by the 973 program (Grant No. 2013CB328704), the NSFC (Grants No. 61435001, No. 11222440, and No. 11474011), the Beijing Natural Science Foundation Program (Grant No. 4132058), and RFDPH (Grant No. 20120001110068). S.A. was supported by NSF award ECCS 1303499. Y.H. acknowledges support from the Chun-Tsung Scholar Fund for Undergraduate Research of Peking University. C.-Y.M. acknowledges support from the President's Fund for Undergraduate Research of Peking University.

[1] K. J. Vahala, Nature (London) **424**, 839 (2003).
[2] V. S. Ilchenko and A. B. Matsko, IEEE J. Sel. Top. Quantum Electron. **12**, 15 (2006).
[3] L. He, S. K. Ozdemir, and L. Yang, Laser Phontonics Rev. **7**, 60 (2013).
[4] D. W. Vernooy, A. Furusawa, N. Ph. Georgiades, V. S. Ilchenko, and H. J. Kimble, Phys. Rev. A **57**, R2293 (1998).
[5] A. Kiraz, P. Michle, C. Becher, B. Gayral, A. Imamoglu, L. Zhang, E. Hu, W. V. Schoenfeld, and P. M. Petroff, Appl. Phys. lett. **78**, 3932 (2001).
[6] T. Aoki, B. Dayan, E. Wilcut, W. P. Bowen, A. S. Parkins, T. J. Kippenberg, K. J. Vahala, and H. J. Kimble, Nature (London) **443**, 671 (2006).
[7] Y.-S. Park, A. K. Cook, and H. Wang, Nano Lett. **6**, 2075 (2006).

[8] K. Srinivasan and O. Painter, Phys. Rev. A **75**, 023814 (2007).

[9] K. Srinivasan and O. Painter, Nature (London) **450**, 862 (2007).

[10] Y.-C. Liu, Y.-F. Xiao, B.-B. Li, X.-F. Jiang, Y. Li, and Q. Gong, Phys. Rev. A **84**, 011805(R) (2011).

[11] Y.-C. Liu, X. Luan, H.-K. Li, Q. Gong, C. W. Wong, and Y.-F. Xiao, Phys. Rev. Lett. **112**, 213602 (2014).

[12] I. Shomroni, S. Rosenblum, Y. Lovsky, O. Bechler, G. Guendelman, and B. Dayan, Science **345**, 903 (2014).

[13] S. Gotzinger, O. Benson, and V. Sandoghdar, Opt. Lett. **27**, 80 (2002).

[14] J. Zhu, S. K. Ozdemir, Y.-F. Xiao, L. Li, L. He, D.-R. Chen, and L. Yang, Nat. Photonics **4**, 46 (2010).

[15] H. Li, Y. Guo, Y. Sun, K. Reddy, and X. Fan, Opt. Express **18**, 25081 (2010).

[16] X. Yi, Y.-F. Xiao, Y.-C. Liu, B.-B. Li, Y.-L. Chen, Y. Li, and Q. Gong, Phys. Rev. A **83**, 023803 (2011).

[17] J. Wiersig, Phys. Rev. A **84**, 063828 (2011).

[18] X.-C. Yu, Y.-C. Liu, M.-Y. Yan, W.-L. Jin, and Y.-F. Xiao, Phys. Rev. A **86**, 043833 (2012).

[19] A. Mazzei, S. Götzinger, L. de S. Menezes, G. Zumofen, O. Benson, and V. Sandoghdar, Phys. Rev. Lett. **99**, 173603 (2007).

[20] S. Arnold, M. Khoshsima, I. Teraoka, S. Holler, and F. Vollmer, Opt. Lett. **28**, 272 (2003).

[21] F. Vollmer and S. Arnold, Nat. Methods **7**, 591 (2008).

[22] D. S. Weiss, V. Sandoghdar, J. Hare, V. Lefvre-Seguin, J.-M. Raimond, and S. Haroche, Opt. Lett. **20**, 1835 (1995).

[23] T. J. Kippenberg, S. M. Spillane, and K. J. Vahala, Opt. Lett. **27**, 1669 (2002).

[24] Y. Shen, D.-R. Chen, and J.-T. Shen, Phys. Rev. A **85**, 063808 (2012).

[25] S. Li, L. Ma, S. Bottner, Y. Mei, M. R. Jorgensen, S. Kiravittaya, and O. G. Schmidt, Phys. Rev. A **88**, 033833 (2013).

[26] J. Zhu, S. K. Özdemir, L. He, and L. Yang, Opt. Express **23**, 23535 (2010).

[27] J. Wiersig, Phys. Rev. Lett. **112**, 203901 (2014).

[28] S. K. Özdemir, J. Zhu, L. He, and L. Yang, Phys. Rev. A **83**, 033817 (2011).

[29] T. J. Kippenberg, A. L. Tchebotareva, J. Kalkman, A. Polman, and K. J. Vahala, Phys. Rev. Lett. **103**, 027406 (2009).

[30] Q. J. Wang, C. Yan, N. Yu, J. Unterhinninghofen, J. Wiersig, C. Pfllül, L. Diehl, T. Edamura, M. Yamanishi, H. Kan, and F. Capasso, Proc. Natl. Acad. Sci. USA **107**, 22407 (2010).

[31] Q. Song and H. Cao, Opt. Lett. **36**, 103 (2011).

[32] Y.-C. Liu, Y.-F. Xiao, X.-F. Jiang, B.-B. Li, Y. Li, and Q. Gong, Phys. Rev. A **85**, 013843 (2012).

[33] F. Vollmer, S. Arnold, and D. Keng, Proc. Natl. Acad. Sci. USA **105**, 20701 (2008).

[34] C.-Y. Chao and L. J. Guo, Appl. Phys. Lett. **83**, 1527 (2003).

[35] J. D. Swaim, J. Knittel, and W. P. Bowen, Appl. Phys. Lett. **102**, 183106 (2013).

[36] L. He, S. K. Ozdemir, J. Zhu, W. Kim, and L. Yang, Nat. Nanotechnol. **6**, 428 (2011).

[37] B.-B. Li, W. R. Clements, X.-C. Yu, K. Shi, Q. Gong, and Y.-F. Xiao, Proc. Natl. Acad. Sci. USA **111**, 14657 (2014).

[38] M. A. Santiago-Cordoba, S. V. Boriskina, F. Vollmer, and M. C. Demirel, Appl. Phys. Lett. **99**, 073701 (2011).

[39] V. R. Dantham, S. Holler, C. Barbre, D. Keng, V. Kolchenko, and S. Arnold, Nano Lett. **13**, 3347 (2013).

[40] S. I. Shopova, R. Rajmangal, S. Holler, and S. Arnold, Appl. Phys. Lett. **98**, 243104 (2011).

[41] J. D. Swaim, J. Knittel, and W. P. Bowen, Appl. Phys. Lett. **99**, 243109 (2011).

[42] V. R. Dantham, S. Holler, V. Kolchenko, Z. Wan, and S. Arnold, Appl. Phys. Lett. **101**, 043704 (2012).

[43] Y.-F. Xiao, Y.-C. Liu, B.-B. Li, Y.-L. Chen, Y. Li, and Q. Gong, Phys. Rev. A **85**, 031805(R) (2012).

[44] T. Lu, H. Lee, T. Chen, S. Herchak, J. H. Kim, S. E. Fraser, R. C. Flagan, and K. Vahala, Proc. Natl. Acad. Sci. USA **108**, 5976 (2011).

[45] J. Knittel, J. D. Swaim, D. L. McAuslan, G. A. Brawley, and W. P. Bowen, Sci. Rep. **3**, 2974 (2013).

[46] Q. Deng, X. Li, Z. Zhou, and H. Yi, Photonics Res. **2**, 71 (2014).

[47] L. Shao, X.-F. Jiang, X.-C. Yu, B.-B. Li, W. R. Clements, F. Vollmer, W. Wang, Y.-F. Xiao, and Q. Gong, Adv. Mater. **25**, 5616 (2013).

[48] L. Chantada, N. I. Nikolaev, A. L. Ivanov, P. Borri, and W. Langbein, J. Opt. Soc. Am. B **25**, 1312 (2008).

[49] D. K. Armani, T. J. Kippenberg, S. M. Spillane, and K. J. Vahala, Nature **421**, 925 (2003).

[50] S. Arnold, D. Keng, S. I. Shopova, S. Holler, W. Zurawsky, and F. Vollmer, Opt. Express **17**, 6230 (2009).

[51] C. W. Gardiner and P. Zoller, *Quantum Noise*, 3rd ed. (Springer, Berlin, 2004).

[52] J. Zhu, S. K. Ozdemir, and L. Yang, in *CLEO: Science and Innovations*, OSA Technical Digest (Optical Society of America, San Diego, CA, 2013), paper CM2H.5.

[53] M. R. Foreman, W.-L. Jin, and F. Vollmer, Opt. Express **22**, 005491 (2014).

[54] J. Zhu, S. K. Ozdemir, L. He, D. Chen, and L. Yang, Opt. Express **19**, 016195 (2011).

[55] S. Arnold, V. R. Dantham, C. Barbre, B. A. Garetz, and X. Fan, Opt. Express **20**, 26147 (2012).

[56] C. F. Bohren and D. R. Huffman, *Absorption and Scattering of Light by Small Particles* (Wiley, New York, 1983).